

Scalable Fabrication of Porous Microchannel Nerve Guidance Scaffolds with Complex Geometries

Dena Shahriari, Gabriel Loke, Ian Tafel, Seongjun Park, Po-Han Chiang, Yoel Fink, and Polina Anikeeva*

Microchannel scaffolds accelerate nerve repair by guiding growing neuronal processes across injury sites. Although geometry, materials chemistry, stiffness, and porosity have been shown to influence nerve growth within nerve guidance scaffolds, independent tuning of these properties in a high-throughput manner remains a challenge. Here, fiber drawing is combined with salt leaching to produce microchannels with tunable cross sections and porosity. This technique is applicable to an array of biochemically inert polymers, and it delivers hundreds of meters of porous microchannel fibers. Employing these fibers as filaments during 3D printing enables the production of microchannel scaffolds with geometries matching those of biological nerves, including branched topographies. Applied to sensory neurons, fiber-based porous microchannels enhance growth as compared to non-porous channels with matching materials and geometries. The combinatorial scaffold fabrication approach may advance the studies of neural regeneration and accelerate the development of nerve repair devices.

Porous scaffolds with precise microstructures and geometries have benefitted from decades of refinement for a diversity of applications ranging from gas separation,^[1,2] water filtration,^[3] cell sorting,^[4] and tissue regeneration.^[5] Applied to nerve repair, these scaffolds are hypothesized to help maintain the organization of nerve bundles and linearly guide growing axons toward their pre-existing targets to restore injured neural pathways

(Figure 1a).^[6,7] Clinically available nerve guidance implants, however, are either limited in length, which reduces their utility in large (>4 cm) gap injuries,^[8] or mechanical flexibility,^[8] which can lead to adverse tissue response and pain. Furthermore, clinically available synthetic channels consist of a single lumen, which does not permit preservation of microstructural organization of nerve fibers and growing axons.^[9] This, in turn, may result in limited or erroneous innervation of distal targets impeding functional recovery and resulting in formation of painful neuropathies.^[10]

To preserve the nerve fiber topography during growth, scaffolds containing multiple individual microchannels have been produced via molding, extrusion, freeze drying, 3D printing, electrospinning, or photolithography.^[11–15] The enhanced ability of such multichannel scaffolds to preserve directionality of growing neuronal processes has been corroborated in rodent models of peripheral nerve^[16,17] and spinal cord injury.^[18–21] Despite the successes of microchannel scaffolds in research models, their translation to clinical use remains impeded by several technological barriers. First, a fabrication technique compatible with a wide range of materials is

Dr. D. Shahriari, G. Loke, Dr. I. Tafel, Dr. S. Park, Dr. P. H. Chiang,
Prof. Y. Fink, Prof. P. Anikeeva
Research Laboratory of Electronics
Massachusetts Institute of Technology
Cambridge, MA 02139, USA
E-mail: anikeeva@mit.edu

Dr. D. Shahriari, Dr. I. Tafel, Dr. S. Park, Dr. P. H. Chiang, Prof. P. Anikeeva
McGovern Institute for Brain Research
Massachusetts Institute of Technology
Cambridge, MA 02139, USA

G. Loke, Prof. Y. Fink, Prof. P. Anikeeva
Department of Materials Science and Engineering
Massachusetts Institute of Technology
Cambridge, MA 02139, USA

Dr. I. Tafel
Department of Neurosurgery
Brigham and Women's Hospital
Boston, MA 02115, USA

Dr. S. Park
Department of Electrical Engineering and Computer Science
Massachusetts Institute of Technology
Cambridge, MA 02139, USA

Prof. Y. Fink
Institute for Soldier Nanotechnologies
Massachusetts Institute of Technology
Cambridge, MA 02139, USA

Prof. Y. Fink
Advanced Functional Fabrics of America
Cambridge, MA 02139, USA

Prof. P. Anikeeva
Department of Brain and Cognitive Sciences
Massachusetts Institute of Technology
Cambridge, MA 02139, USA



The ORCID identification number(s) for the author(s) of this article can be found under <https://doi.org/10.1002/adma.201902021>.

DOI: 10.1002/adma.201902021

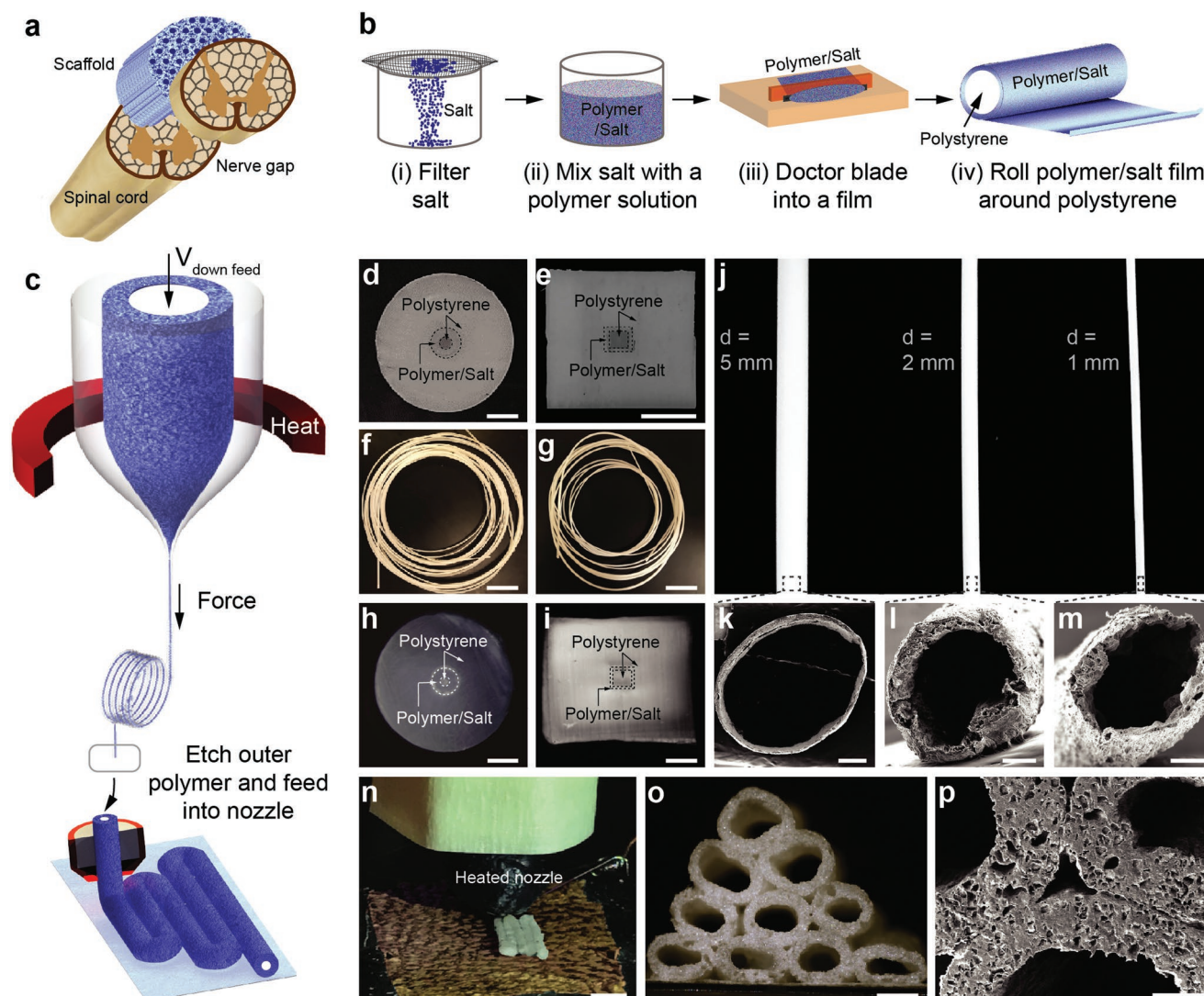


Figure 1. Fabrication steps of porous microchannel scaffolds with complex geometries. a) A schematic of a spinal cord nerve gap injury and a microchannel scaffold with a matching cross section to bridge the gap. b) NaCl crystals are filtered to select grain size and mixed with a polymer solution. The polymer/salt solution is doctor-bladed into films, then rolled and consolidated around a polystyrene rod used as a sacrificial material. c) The composite preform is inserted into a sacrificial cladding from the same material as the core, thermally drawn and fed into a heated nozzle for fuse-printing. d,e) Cross-sectional photographs of preforms containing PCL/NaCl composite and polystyrene sacrificial core and cladding with circular (d) and rectangular (e) cross sections. f,g) Meter-long sections of circular and rectangular fibers produced from the preforms in (d) and (e), respectively. Scale bars = 10 mm. h,i) Cross-sectional micrographs of the fibers drawn from the preforms shown in (d) and (e), respectively. Scale bars = 300 μm . j) Hollow channel fibers produced from the preform in (d) with varying diameters following removal of the sacrificial cladding. The tuning of the channel diameter is achieved by varying the preform feed speed and drawing speed. k–m) SEM images of the hollow fibers in (j). The scale bars in (k), (l), and (m) are 500, 200, and 100 μm , respectively. n) Following removal of the sacrificial core and cladding, the channel fibers are passed through a heated nozzle to fuse-print scaffolds with complex geometries. The color of the bottom surface is modified from the original to facilitate visualization. Scale bar = 3 mm. o) A fuse-printed microchannel scaffold with a digitally imparted geometry. Scale bar = 300 μm . p) A close-up SEM image of an interface between three porous channels within a fuse-printed scaffold. Scale bar = 150 μm .

required to optimize the scaffolds' mechanical and chemical properties for enhanced biocompatibility and improved nerve growth.^[14] Second, to enable the transport of nutrients, oxygen, and waste, materials constituting the scaffold walls should support interconnected porosity.^[22,23] Third, the scaffold geometry should resemble the structural complexity of the injured nerve.^[24,25] Fourth, to facilitate translation of synthetic scaffolds from bench to bedside, these devices must be reproducibly manufactured at lengths corresponding to clinically observed

nerve gaps with a diversity of cross-sectional dimensions and geometries.

To overcome these technical barriers, we introduce a high-throughput fabrication technique that delivers microchannel scaffolds with flexibility over constituent materials and device dimensions and controlled porosity and digitally pre-defined geometries. Our method relies on thermal drawing of macroscopic multimaterial models, preforms, into microstructured multifunctional fibers.^[26] Preforms with centimeter-scale lateral

dimensions and lengths, composed of multiple materials with similar glass transition (T_g) and melting (T_m) temperatures can be produced via conventional machining and assembly techniques, and then drawn into tens to thousands of meters of fibers with micro-scale lateral dimensions and cross-sectional geometries matching those of the preforms.^[27–32] Although thermal drawing readily delivers microscale devices at high yield, fabrication of porous structures via this method poses a challenge, as pores cannot be programmed at the preform level. Porosity in thermally drawn fibers was recently achieved by leveraging thermally induced phase segregation of a polymer-solvent mixture.^[31] This approach, however, imposes restrictions on materials selection and couples pore dimensions to the polymer and solvent properties.

To expand the use of fiber drawing to a wide array of thermoplastics and to precisely control pore sizes, we employed a porogen (sodium chloride, NaCl) loaded into polymers prior to the preform fabrication (Figure 1b). NaCl crystals with the desired dimensions were obtained via filtration and mixed with solutions of thermoplastics that were then cast into films of defined thickness by doctor-blading. For each device, the composite polymer-NaCl films were then rolled around a mandrel of a sacrificial material with a T_g close to that of the polymer composite and consolidated under heat. The resulting structures were inserted into a sacrificial cladding of the material matching that of the sacrificial core and thermally drawn into tens of meters of microstructured fibers with circular and rectangular cross sections (Figure 1c–i). Following thermal drawing, the sacrificial polymer cladding and core and the NaCl crystals were sequentially dissolved by selective chemical etching resulting in porous microchannels with linear dimensions defined by the preform geometry and drawing parameters (Figure 1d–i). Lateral dimensions of the microchannels could be tuned by varying the stress on the fiber during thermal drawing (Figure 1j–m). The thermally drawn composite fibers could then be 3D fuse-printed into complex geometries (Figure 1n–p).

As our approach is largely agnostic to the chemistry of the thermoplastic, we applied it to polycaprolactone (PCL) and polylactic acid (PLA) both of which are ubiquitously used in tissue engineering.^[33,34] Tens of meters of hollow PCL and PLA constructs with circular and rectangular cross sections, inner core dimensions ranging between 50 μm and 3 mm, and wall thicknesses tunable between 20 μm and 1 mm were produced (Figure 2a–f; Figure S1a,b, Supporting Information).

Pore dimensions and their distribution corresponded to those of the NaCl porogen crystals embedded within the polymer matrix (Figure 2g,h). To enable fluid exchange between the neurites growing within the fiber scaffolds and the exterior environment, while avoiding non-directional growth through the pores, the dimensions of the latter should be <100 μm .^[35] To further prevent the neuronal migration through the pores we selected NaCl crystals with a size of $11.4 \pm 5.26 \mu\text{m}$ (mean \pm standard deviation (SD)) as a porogen for the remainder of our study. To obtain interconnected porosity, numerical analysis estimated the percolation threshold with highly irregular particles (20 faces particle) of similar dimensions to be approximately 30%.^[36] We discovered that, while it was possible to produce thermally drawn PCL filaments with porosity exceeding

45 vol%, such structures could not be easily handled or fuse-printed. The PCL filaments with 35 vol% porosity, however, were mechanically robust and suitable for fuse-printing.

To verify interconnected porosity and to determine the time necessary for complete salt removal, we applied elemental dispersion X-ray (EDX) analysis to the PCL channels fabricated with 35 vol% salt. Sacrificial claddings and inner cores were dissolved from 1 cm-long sections of cylindrical PCL channels with an inner diameter of 300 μm and wall thickness of 78 μm . The EDX analysis was performed on the midline cross sections (0.5 cm from each end) of the channels, revealing an average of 20.7% and 96.9% removal of salt following 1 and 24 h in water bath, respectively (Figure 2i–n). In addition, as theoretically predicted^[37] and experimentally reported for PCL films,^[38] introducing pores reduced the elastic moduli of PCL channels. Tensile testing of PCL channels indicated a decrease in the elastic moduli from 294.3 kPa for solid PCL to 70.0 kPa for PCL with 35 vol% porosity.

While microscale single lumen channels enable nerve guidance in vitro, they have limited utility in repairing nerves with complex architectures in vivo. Consequently, we sought to produce porous scaffolds with multiple inner channels with complex targeted outer geometries, without restrictions on length or cross-sectional dimensions. This was accomplished by applying a filament surface heating technique to 3D print the thermally drawn conduits into digitally defined shapes. Akin to thermal drawing, filament surface heating can be applied to a broad range of thermoplastics enabling the combinatorial processing of materials via sequential use of the two techniques.

Prior to fuse-printing of scaffold structures, the sacrificial polystyrene cladding was chemically etched off the PCL fibers to produce hollow channels. The NaCl crystals, however, were left within the polymer matrix to avoid potential collapse of the pores during the surface heating. The conduits were then fed into a printing nozzle where the surface heating occurred, which resulted in the fusion of adjacent microchannel fibers (Figure S2, Supporting Information). The printed structures were then subjected to salt-leaching to produce multichannel microporous scaffolds at centimeter scales. To illustrate the utility of our approach to produce complex structures, we printed multichannel scaffolds with cross-sectional geometries mimicking that of the spinal cord cross section as well as bifurcated scaffolds that could potentially be applied to bridge transected branched nerves (Figure 3a,b; Figure S3a, Supporting Information). Following salt leaching, scanning electron microscopy (SEM) images of the fuse-printed scaffolds revealed their porous walls analogous to those of the individual fiber channels (Figure 3c,d).

To evaluate the utility of the porous microchannel fibers as conduits for nerve growth, we first evaluated their stability in physiological conditions. Scaffold shapes and pore sizes were maintained over 28 days in phosphate buffered saline under gentle agitation at 37 °C (Figure 3e,f; Figure S3b, Supporting Information). Furthermore, an AlamarBlue cytotoxicity assay applied to human embryonic kidney (HEK293) cells cultured in media containing the scaffolds did not reveal any adverse effects on the cell viability (Figure S4, Supporting Information).

The necessity of porous walls for nerve growth within scaffold channels is widely accepted in tissue engineering as

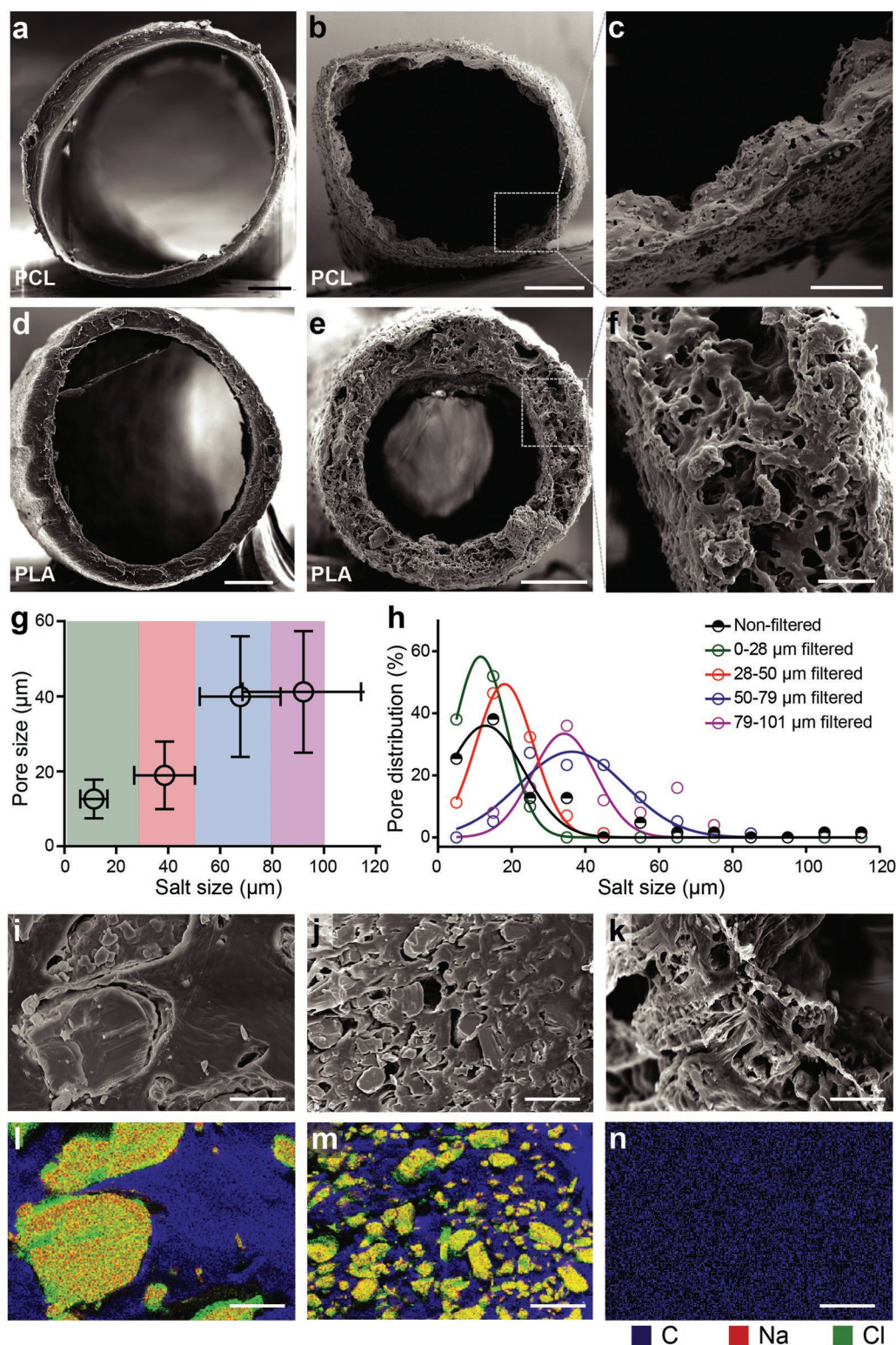


Figure 2. Porosity in thermally drawn microchannel fibers. a) Non-porous and b) porous PCL fiber channels. Scale bars = 100 μm . c) A magnified image of the dashed box shown in (b). Scale bar = 40 μm . d) Non-porous and e) porous PLA fiber channels. Scale bars = 100 μm . f) An image of the dashed box shown in (e). Scale bar = 40 μm . g) The average sizes of NaCl crystals used for PCL channel fabrication correlated to the average pore sizes. Bars indicate SD. The shaded areas mark the sizes of the meshes used to filter NaCl crystals. h) Pore distributions in fiber channels produced from PCL composites with NaCl crystals of different size ranges. i–k) SEM and l–n) EDX analysis of PCL composites. i,l) Images prior to salt-leaching. j,m) Images following one hour of salt-leaching. k,n) Images following 24 h following salt-leaching. Carbon (C) is marked as blue, Na as red and Cl as green (yellow color corresponds to NaCl). Scale bars = 30 μm .

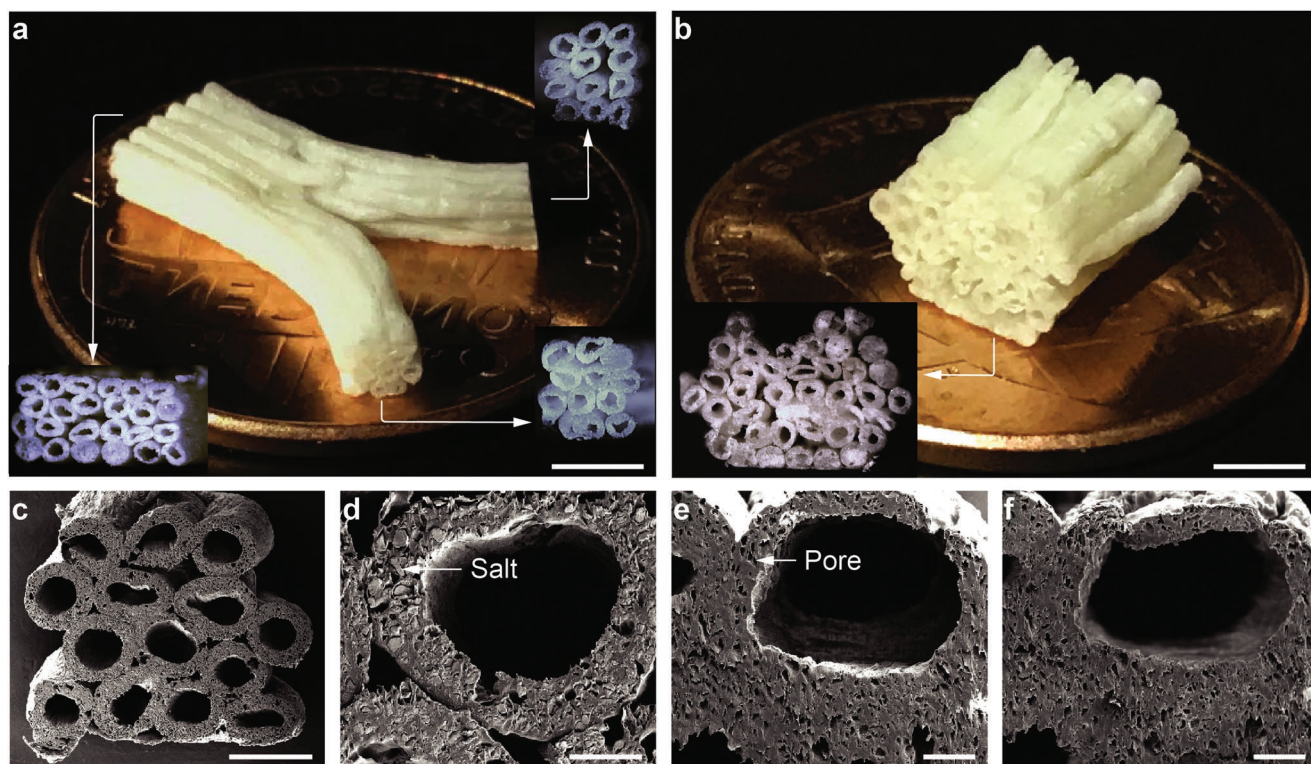


Figure 3. 3D-printed scaffolds. Photographs of a) branched and b) butterfly-shaped fuse-printed scaffolds mimicking a bifurcated nerve and spinal cord cross section, respectively. Scale bars = 2 mm. c) A SEM image of a hexagonally packed printed scaffold. Scale bar = 1 mm. d,e) SEM images prior to (d) and following (e) salt-leaching demonstrates salt particle removal and emergence of porosity. f) A SEM image of a printed porous scaffold following 4-week incubation in physiological conditions (phosphate buffered saline, 37 °C) under gentle agitation. The structure maintained porosity and adhesion between the individual microchannel fibers. d–f) Scale bars = 200 μ m.

the porosity facilitates adequate nutrient, waste, and oxygen exchange between the tissue and the local environment.^[39] We sought to evaluate the effects of porosity on nerve growth within our thermally drawn microchannels *in vitro*. Consistent with prior studies,^[40] primary neonatal rat dorsal root ganglia (DRGs) were used as an *in vitro* model of peripheral nerve growth within the scaffolds. Isolated DRGs were cut in half, and placed at the edges of porous and non-porous thermally drawn PCL channels coated with Matrigel. 12 days following seeding, DRGs placed within the porous channels exhibited longer processes than those placed within non-porous structures as revealed by neurofilament (NF) immunostaining ($p < 0.05$; post hoc Tukey HSD test, **Figure 4a,b**). Consistent with prior reports, the migration and growth of Schwann cells, as quantified by S-100 immunostaining, accompanied neurite extension (Figure S5, Supporting Information).^[41,42] To test if the nerve growth was reduced within non-porous channels due to lower mass transport or due to the differences in surface morphology, DRGs were also cultured on Matrigel-coated porous and non-porous PCL films and glass coverslips as controls submerged in media with no restrictions on mass transport. In contrast to the findings for nerve guidance channels, similar growth ($p > 0.05$; post hoc Tukey HSD test) was observed for both films (Figure 4c,d; Figures S5 and S6, Supporting Information), which suggested that mass transport played a more significant role in confined environments. In both porous and non-porous channels, the neurite outgrowth from DRGs extended

significantly beyond the lengths observed for DRGs seeded on films ($p < 0.05$; post hoc Tukey HSD test, Figure 4e).

The combination of fiber drawing and salt-leaching enabled high-throughput fabrication of nerve guidance channels with controlled porosity, stiffness, and dimensions from different thermoplastics. These porous fiber-based channels were further arranged into complex scaffold geometries via filament surface heating fuse-printing. As the latter method takes advantage of digital design, it may enable fabrication of personalized patient-specific scaffolds based on the structural images of injured nerves. Our scalable approach for producing porous structures with pre-defined geometries and lengths may find additional applications outside tissue engineering including fluid filtration and chemical separation.

Experimental Section

Conduit Fabrication via Thermal Drawing: NaCl (Alfa Aesar) was ground using an automatic ceramic mortar and pestle (Fritsch). Nylon filter meshes with sizes of 28, 50, 79, and 101 μ m (McMaster) were then used to select salt particles with size ranges of <28, 28–50, 50–79, and 79–101 μ m by first shaking dry over the smaller size mesh and then the mesh with the upper size, when applicable. PCL (MilliporeSigma) was dissolved in chloroform to form a 3 wt% solution. PLA (GoodFellow) was dissolved in a 50:50 volume ratio chloroform and dichloromethane and a 4 wt% solution was obtained. The polymer solutions were mixed with salt at the desired size range and volume percentages (up to 65 vol% salt) using a vortex (VWR). A T-shape aluminum (Al) piece was

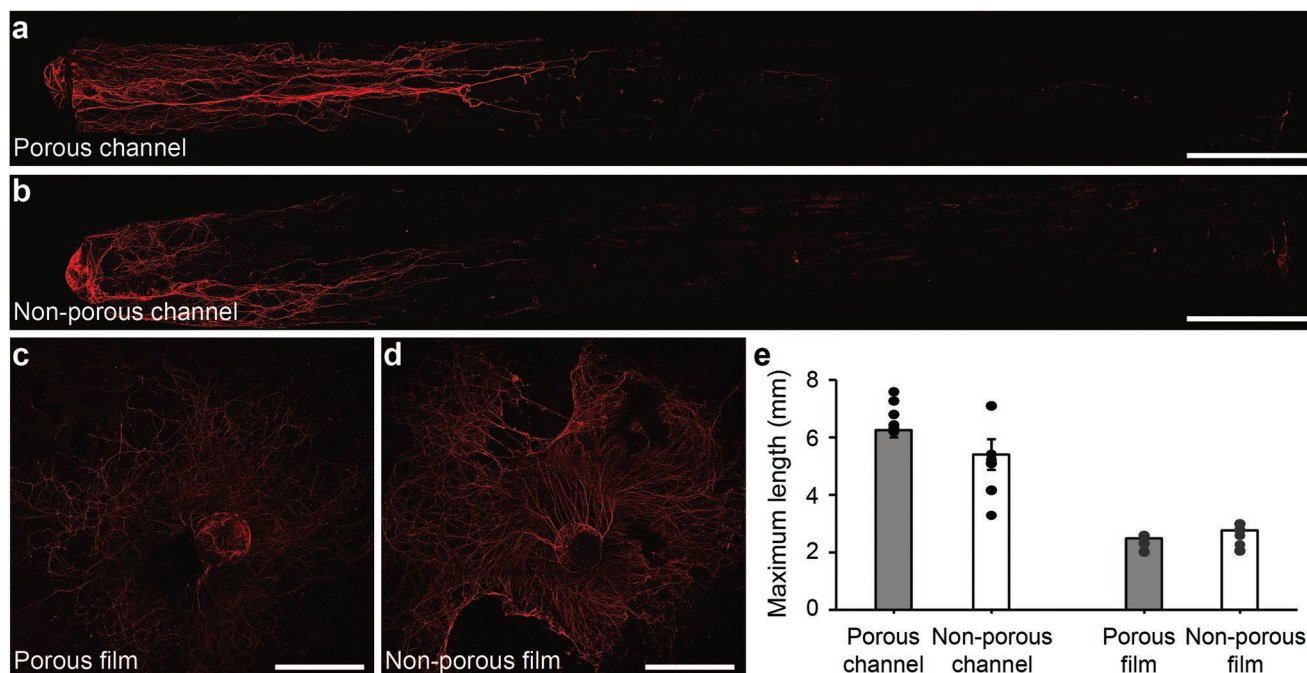


Figure 4. Neurite outgrowth from isolated DRGs following 12 days in vitro. a,b) Confocal microscopy images of immunostaining for neurofilaments demonstrate neurite extension within porous (a) and non-porous (b) PCL fiber channels. c,d) Confocal images of the neurite extension, as marked by neurofilament immunostaining, from DRGs seeded on porous (c) and non-porous (d) PCL films. e) Neurite extension between the four groups was compared by a two-way ANOVA followed by post hoc Tukey HSD test. Average neurite extension is greater in porous PCL channels than in non-porous channels ($n = 7$ samples for porous channels and $n = 6$ samples for non-porous channels; $p < 0.05$). Neurite extension is significantly greater in channels than on flat PCL films independent of porosity ($n = 6$ samples; $p < 0.05$). No significant differences are found in neurite extension on porous and non-porous films ($p > 0.05$). All values are mean \pm standard error of mean. All scale bars are 1 mm.

machined to a blade with a height of 1 mm for doctor blading. Polymer/salt mixtures were poured on a copper sheath for PCL and glass for PLA, and the Al blade was passed over the mixtures. The films were air-dried for at least 10 min for PCL and 30 min for PLA prior to removal. Film removal was aided by applying ethanol to the films. The solvents were removed in vacuum for over 24 and 48 h for PCL and PLA, respectively. The films were wrapped around polystyrene (PS; McMaster) with circular or square cross sections and covered with a Teflon sheath which was then tightly taped. A uniform piece was obtained by consolidating the films around the rod in an oven at the following temperatures for 30 min: 100% PCL at 63 °C, PCL/salt at 70 °C, 100% PLA at 73 °C, and PLA/salt at 80 °C. The consolidated rods, were then placed inside a 25.4 mm diameter PS rod after machining it to have a hole in the middle with the size of the outer diameter of the consolidated rod (between 4 mm and 9 mm). For square cross-sectional fibers, machined PS slabs with consolidated PCL/PS pieces were placed in a press at 100 °C for 1 h and then, while preserving the temperature, a pressure of 50 psi was applied for 1 h. The preform was then air-cooled to room temperature under pressure. During thermal drawing, preforms were vertically suspended inside a furnace at 220 °C for PCL and 240 °C for PLA. To remove the PS, conduits were placed in cyclohexane under gentle agitation (<50 rotation per minute) overnight. The samples were then first rinsed with ethanol (VWR) and then placed in water for at least 24 h to remove the salt.

Conduit Characterization: Conduits were cut with razor blades and coated with 3 nm of gold particles and imaged with SEM (Model 6010LA; JOEL). Salt and pore size quantification were done with ImageJ software. For EDX analysis, thermally drawn PCL conduits with 35 vol% salt and an inner diameter of 0.3 mm were cut to 10 mm in length. After etching the PS in cyclohexane overnight, the samples were used as they were or rinsed with ethanol and placed in water for 1 or 24 h. All samples were cut in half, gold coated and assessed for NaCl presence using EDX (Model 6010LA; JOEL) ($n = 3$). Tensile testing was done on

non-porous and 35 vol% porous PCL conduits of 15 mm in length and 0.3 mm inner diameter in a dynamic mechanical analyzer (Model DMA Q800; TA Instruments) under a constant extension rate of 0.2 mm min⁻¹ ($n = 5$) until conduit breakage.

Fuse-Printing Microchannel Scaffolds and Analysis: PCL fibers with 35 vol% porosity were thermally drawn as described above. About 5–7 m of the fibers with 0.3 mm inner diameter were placed in cyclohexane for 12 h, with the solution changed three times for the outer polystyrene to be completely removed, while the inner polystyrene was only partially removed. The fibers were subsequently fed into a printing nozzle. The nozzle contained a short stainless steel hot end with a length of 0.3 mm to heat the fibers. The diameter of the hot end was 0.8 mm, which corresponded to the fiber outer diameter of 0.7–0.8 mm. The hot end temperature was 165–175 °C, measured by a VWR thermocouple probe. The feeding speed was 100–120 mm min⁻¹. The PCL fibers were printed onto an underlying PCL film (thickness of 0.2 mm) for adhesion of the first printed layer to the print bed. The input layer height was set as the diameter of the fiber. The 3D design of the porous scaffold was drawn in Solidworks and was later processed by Slic3r to create a gcode for printing. The gcode of the printed scaffold was then read by Pronterface software, which communicated the required XYZ print positions to the 3D-printer (Rova3D Multinozzle printer). The scaffold characterization and quantifications were done via SEM imaging and imageJ, respectively. Cytotoxicity tests were done via AlamarBlue (ThermoFisher) assays on HEK cells following the manufacturer's protocol.

DRG Isolation: All animal handling and procedures were approved by the MIT Committee on Animal Care and were in compliance with the National Institutes of Health Guide for the Care and Use of Laboratory Animals. DRGs were isolated from Sprague Dawley neonatal rats on postnatal day 1 (Charles River). Individual DRG explants were collected from the spinal column, and the nerve roots and connective tissue were removed from the DRGs.

In Vitro Setup and Immunohistochemistry: Non-porous and 35 vol% porous PCL conduits were sectioned to 10 mm in length. After the polystyrene and salt were removed as described above, the conduits and PCL films with similar porosities to those of conduits were placed in ethanol and set in the biosafety cabinet under UV for 45 min. Maintaining the samples sterile, ethanol was replaced with sterilized phosphate buffer saline (1xDPBS) and exchanged three times, letting it rest for 15 min each time, and then air-dried. In vitro studies were performed similar to a previous study.^[32] Briefly, samples were coated with Matrigel by applying reduced growth factor Matrigel (BD Biosciences) at a 1:30 dilution with a DRG medium (Neurobasal-A media supplemented with B-27 and glutamax; Life Technologies) for an hour at room temperature. The coated conduits and films were placed in a DRG medium in non-tissue culture 24-well plates (VWR Scientific Products) for at least 2 h. During this time, air bubbles were pressed out of the conduits using sterile tweezers. For the control experiments, 12-mm glass coverslips (Electron Microscopy Sciences) etched overnight in 10% hydrochloric acid solution (Sigma) and stored in 99% ethanol were used. The coverslips were dried over a flame and placed into 24-well plates and coated with Matrigel as described above. The isolated DRGs were sectioned in half and either placed inside the conduits at one end, or in the center of the films/coverslips. The media was changed every 3–4 days and the cultures were fixed on day 12 with 4% paraformaldehyde (Electron Microscopy Sciences) in 1xDPBS for 40 min. The samples were then rinsed with 1xDPBS and permeabilized with 0.1% Triton X-100 in 1xPBS for 25 min. Goat serum (2.5%) was used to block the samples at 4 °C overnight. Samples were then incubated in 1:500 rabbit anti-neurofilament primary antibody (N4142, MilliporeSigma) and 1:500 mouse anti-S100 (S2657, MilliporeSigma) diluted in 2.5% donkey serum for 2 h at room temperature, and rinsed three times in 1xPBS for 15 min each. Secondary antibody staining was done with 1:1000 goat anti-rabbit Alexa Fluor 633 IgG (A21070, Life Technologies) and 1:1000 goat anti-mouse Alexa Fluor 568 IgG (A11004, Life Technologies) for 2 h, followed by three washes in 1xDPBS of 15 min each. To stain the nuclei, the samples were then incubated with 30 µm 6-diamidino-2-phenylindol (DAPI) (Life Technologies) for 2 min and washed with 1xDPBS three times. The samples were mounted on glass slides with VECTASHIELD mounting medium containing 6-diamidino-2-phenylindol (DAPI; VWR). Slides were imaged with a confocal microscope (Olympus FV1000 laser scanning confocal microscope). The maximum length of neurite growth from the center of the ganglia at the edge of the channels were used for analyzing growth in channels. Neurite growth length on the films was determined as the average radius of the neurite growth from the center of the ganglia to the end points generated by 72 cross-sectional lines with 5° spacing. Neurite extension were quantified via ImageJ. Statistical analysis was done in Python.

Supporting Information

Supporting Information is available from the Wiley Online Library or from the author.

Acknowledgements

This work was supported in part by the National Institute of Neurological Disorders and Stroke (5R01NS086804, P.A.), National Science Foundation (NSF) Center for Materials Science and Engineering (DMR-1419807, P.A. and Y.F.), NSF Center for Neurotechnology (EEC-1028725, P.A.), the McGovern Institute for Brain Research at MIT (P.A.), and the U.S. Army Research Office through the Institute for Soldier Nanotechnologies at MIT (W911NF-13-D-0001, Y.F.). D.S. is a recipient of the Craig Nielsen postdoctoral fellowship. S.P. was a recipient of Samsung Scholarship. The authors thank Dr. Siyuan Rao for her help with figure preparation and advice on statistical analysis and Dr. Andres

Canales for his advice on statistical analysis and helpful comments on the manuscript.

Conflict of Interest

The authors declare no conflict of interest.

Keywords

3D printing, nerve guidance scaffolds, nerve repair, porous fibers, thermal drawing

Received: March 30, 2019

Revised: May 15, 2019

Published online:

- [1] J. Duan, W. Jin, S. Kitagawa, *Coord. Chem. Rev.* **2017**, *332*, 48.
- [2] G. Maurin, C. Serre, A. Cooper, G. Férey, *Chem. Soc. Rev.* **2017**, *46*, 3104.
- [3] H. Yuan, Z. He, *Bioresour. Technol.* **2015**, *195*, 202.
- [4] M. S. Jeon, Y. Jeon, J. H. Hwang, C. S. Heu, S. Jin, J. Shin, Y. Song, S. Chang Kim, B.-K. Cho, J.-K. Lee, D. R. Kim, *Carbon* **2018**, *130*, 814.
- [5] F. Bairo, S. Fiorilli, C. Vitale-Brovarone, *Acta Biomater.* **2016**, *42*, 18.
- [6] T. Gros, J. S. Sakamoto, A. Blesch, L. A. Havton, M. H. Tuszynski, *Biomaterials* **2010**, *31*, 6719.
- [7] O. Kiehn, *Nat. Rev. Neurosci.* **2016**, *17*, 224.
- [8] S. Kehoe, X. F. Zhang, D. Boyd, *Injury* **2012**, *43*, 553.
- [9] H. H. Oh, Y.-G. Ko, H. Lu, N. Kawazoe, G. Chen, *Adv. Mater.* **2012**, *24*, 4311.
- [10] T. Führmann, M. S. Shoichet, *Biomed. Mater.* **2018**, *13*, 050201.
- [11] X.-Y. Yang, L.-H. Chen, Y. Li, J. C. Rooke, C. Sanchez, B.-L. Su, *Chem. Soc. Rev.* **2017**, *46*, 481.
- [12] H.-M. Yin, Y.-F. Huang, Y. Ren, P. Wang, B. Zhao, J.-H. Li, J.-Z. Xu, Z.-M. Li, *Compos. Sci. Technol.* **2018**, *156*, 192.
- [13] M. Behbehani, A. Glen, C. S. Taylor, A. Schuhmacher, J. W. Haycock, *Int. J. Bioprint.* **2018**, *4*, 1.
- [14] M. Guvendiren, J. Molde, R. M. D. Soares, J. Kohn, *ACS Biomater. Sci. Eng.* **2016**, *2*, 1679.
- [15] E. Sachlos, J. T. Czernuszka, *Eur. Cells Mater.* **2003**, *5*, 29.
- [16] R. V. Bellamkonda, *Biomaterials* **2006**, *27*, 3515.
- [17] S. Mobini, B. S. Spearman, C. S. Lacko, *Curr. Opin. Biomed. Eng.* **2017**, *4*, 134.
- [18] S. Stokols, J. Sakamoto, C. Breckon, T. Holt, J. Weiss, M. H. Tuszynski, *Tissue Eng.* **2006**, *12*, 2777.
- [19] K. Pawar, R. Mueller, M. Caioni, P. Prang, U. Bogdahn, W. Kunz, N. Weidner, *Acta Biomater.* **2011**, *7*, 2826.
- [20] H. M. Tuinstra, M. O. Aviles, S. Shin, S. J. Holland, M. L. Zelivyanskaya, A. G. Fast, S. Y. Ko, D. J. Margul, A. K. Bartels, R. M. Boehler, B. J. Cummings, A. J. Anderson, L. D. Shea, *Biomaterials* **2012**, *33*, 1618.
- [21] J. Koffler, W. Zhu, X. Qu, P. Oleksandr, J. N. Dulin, J. Brock, L. Graham, P. Lu, J. Sakamoto, M. Marsala, S. Chen, M. H. Tuszynski, *Nat. Med.* **2019**, *25*, 263.
- [22] E. Wintermantel, J. Mayer, J. Blum, K. L. Eckert, P. Lüscher, M. Mathey, *Biomaterials* **1996**, *17*, 83.
- [23] I. Martin, D. Wendt, M. Heberer, *Trends Biotechnol.* **2004**, *22*, 80.
- [24] B. N. Johnson, K. Z. Lancaster, G. Zhen, J. He, M. K. Gupta, Y. L. Kong, E. A. Engel, K. D. Krick, A. Ju, F. Meng, L. W. Enquist, X. Jia, M. C. McAlpine, *Adv. Funct. Mater.* **2015**, *25*, 6205.

- [25] E. B. Petcu, R. Midha, E. Mccoll, A. Popa-wagner, T. V. Chirila, P. D. Dalton, *Biofabrication* **2018**, *10*, 032001.
- [26] W. Yan, A. Page, T. Nguyen-Dang, Y. Qu, F. Sordo, L. Wei, F. Sorin, *Adv. Mater.* **2019**, *31*, 1802348.
- [27] A. Canales, X. Jia, U. P. Froriep, R. A. Koppes, C. M. Tringides, J. Selvidge, C. Lu, C. Hou, L. Wei, Y. Fink, P. Anikeeva, *Nat. Biotechnol.* **2015**, *33*, 277.
- [28] S. Park, Y. Guo, X. Jia, H. Kyoung Choe, B. Grena, J. Kang, J. Park, C. Lu, A. Canales, R. Chen, Y. Shin Yim, G. B. Choi, Y. Fink, P. Anikeeva, *Nat. Neurosci.* **2017**, *20*, 612.
- [29] T. Khudiyev, C. Hou, A. M. Stolyarov, Y. Fink, *Adv. Mater.* **2017**, *29*, 1605868.
- [30] T. Khudiyev, J. Clayton, E. Levy, N. Chocat, A. Gumennik, A. M. Stolyarov, J. Joannopoulos, Y. Fink, *Nat. Commun.* **2017**, *8*, 1435.
- [31] B. Grena, J.-B. Alayrac, E. Levy, A. M. Stolyarov, J. D. Joannopoulos, Y. Fink, *Nat. Commun.* **2017**, *8*, 364.
- [32] R. A. Koppes, S. Park, T. Hood, X. Jia, N. A. Poorheravi, H. Achyuta, Y. Fink, P. Anikeeva, *Biomaterials* **2016**, *81*, 27.
- [33] W. F. A. Den Dunnen, P. H. Robinson, R. Van Wessel, A. J. Pennings, M. B. M. Van Leeuwen, J. M. Schakenraad, *J. Biomed. Mater. Res.* **1997**, *36*, 337.
- [34] D. Angius, H. Wang, R. J. Spinner, Y. Gutierrez-Cotto, M. J. Yaszemski, A. J. Windebank, *Biomaterials* **2012**, *33*, 8034.
- [35] A. Wang, Q. Ao, W. Cao, M. Yu, Q. He, L. Kong, L. Zhang, Y. Gong, X. Zhang, *J. Biomed. Mater. Res., Part A* **2006**, *79A*, 36.
- [36] S. Torquato, Y. Jiao, *Phys. Rev. E* **2013**, *87*, 022111.
- [37] R. M. German, *Powder Metallurgy Science*, 2nd ed., Metal Powder Industries Federation, Princeton, NJ, USA **1994**.
- [38] S. Eshraghi, S. Das, *Acta Biomater.* **2010**, *6*, 2467.
- [39] Q. L. Loh, C. Choong, *Tissue Eng., Part B* **2013**, *19*, 485.
- [40] J. Scheib, A. Höke, *Nat. Rev. Neurol.* **2013**, *9*, 668.
- [41] Y. Kim, V. K. Haftel, S. Kumar, R. V. Bellamkonda, *Biomaterials* **2008**, *29*, 3117.
- [42] S. Tang, J. Zhu, Y. Xu, A. P. Xiang, M. H. Jiang, D. Quan, *Biomaterials* **2013**, *34*, 7086.